CHAPTER

19

Assembly of a simple scalable device for micromechanical testing of plant tissues

Amir J. Bidhendi, M. Shafayet Zamil, and Anja Geitmann*

Department of Plant Science, McGill University, Macdonald Campus, Ste-Anne-de-Bellevue, Québec, Canada

**Corresponding author: e-mail address: geitmann.aes@mcgill.ca*

Chapter outline

Abstract

Tensile testing is widely used to evaluate the mechanical properties of biological materials including soft primary plant tissues. Commercially available platforms for tensile testing are often expensive and limited in customizability. In this chapter, we provide a guide for

Methods in Cell Biology, Volume 160, ISSN 0091-679X, https://doi.org/10.1016/bs.mcb.2020.04.003

the assembly and use of a simple and low-cost micromechanical testing apparatus suitable for research and educational purposes. The build of the setup is presented with scalability and universality in mind and is based on a do-it-yourself mind frame towards mechanical tests on plant organs and tissues. We discuss hardware and software requirements with practical details on required components, device calibration and a script to run the device. Further, we provide an example in which the device was used for the uniaxial tensile test of onion epidermis.

1 Introduction

The plant cell wall resembles a fiber-reinforced composite material composed of polysaccharides, proteins, water, and ions. Our understanding of the molecular interactions of the constituents and the biomechanical behavior of the primary plant cell wall is still evolving (Bidhendi, Altartouri, Gosselin, & Geitmann, 2019; Bidhendi & Geitmann, 2016, 2018a; Cosgrove, 2014; Zhang, Tang, Vavylonis, & Cosgrove, 2019). The mechanical properties of the cell wall play a crucial role in cell growth and tissue morphogenesis and their quantitative measurement is, therefore, integral to developmental studies.

The mechanical properties of plant materials can be measured by probing their deformation behavior in a variety of testing assays (Bidhendi & Geitmann, 2019; Milani, Braybrook, & Boudaoud, 2013; Routier-Kierzkowska & Smith, 2013). Such measurement techniques have greatly assisted in revealing the underlying mechanisms governing plant cell growth and have provided quantitative inputs for theoretical models of cell wall dynamics and behavior leading to novel ideas for further experimental research (McQueen-Mason, Durachko, & Cosgrove, 1992; Tagawa & Bonner, 1957; Wei & Lintilhac, 2007; Wei, Lintilhac, & Tanguay, 2001; Zhang, Vavylonis, Durachko, & Cosgrove, 2017). Furthermore, a quantitative understanding of the mechanical properties and composition of plant materials is vital from the perspectives of crop yield, food quality assessment, or use of plant-based or plant-inspired materials for biomedical applications (Berthaume, 2016; Forell, Robertson, Lee, & Cook, 2015; Pelling & Hickey, 2019; Vega-Sánchez et al., 2012).

The tension assay is a classic mechanical testing method. It is of particular interest in the assessment of mechanical properties of the plant cell wall because tension deforms the plant cell wall in its plane. The direction of load application thus probes the mechanical properties that are more closely relevant to the stresses experienced by the cell walls due to turgor, compared to other types of deformation induced in tests such as indentation (Bidhendi & Geitmann, 2019; Milani et al., 2011; Zhang et al., 2019). Uniaxial tension is invoked by the application of a force resulting in stretching of the sample in one direction. Measurement of the applied force and the deformation of a sample allows the determination of several mechanical parameters, including elastic modulus, creep behavior and viscoelastic properties. For information on the theoretical foundation, and particular applications of tensile testing for plant samples we refer to numerous available articles and textbooks

(e.g., Bidhendi & Geitmann, 2018b, 2019; Bidhendi, Li, & Geitmann, 2019; Chanliaud, Burrows, Jeronimidis, & Gidley, 2002; Cosgrove, 1993, 2016; Davis, 2004; Lynch & Lintilhac, 1997; Robinson & Durand-Smet, 2020; Robinson et al., 2017; Sharpe, 2008; Spatz, Kohler, & Niklas, 1999; Suslov & Verbelen, 2006; Vanstreels et al., 2005; Zamil, Yi, Haque, & Puri, 2013; Zamil, Yi, & Puri, 2015). In this chapter, we present a simple procedure for setting up an affordable mechanical testing device that can be used for a variety of mechanical tests, but we focus on uniaxial tension application performed under a microscope. We discuss hardware and software requirements, provide a custom script for data acquisition, and an example of its use on onion epidermis.

2 Rationale

The power of quantitative data obtained through mechanical testing of plant material has been demonstrated in a variety of plant and cell developmental studies. However, the costs of commercially available testing platforms suitable for delicate plant structures are often prohibitive and their flexibility for customization to specific tissues or testing environments is limited. We believe that affordable, easy to use and customizable tools facilitate the realization of research potentials. In line with this vision, the present guide provides simple instructions to build a mechanical device, with a focus on uniaxial testing applications.

3 Device presentation

The device presented in this chapter allows the execution of a controlled stretch of a longitudinal specimen and measurement of the corresponding force. The setup allows real-time microscopic observation of the sample during the test, which is particularly important for studies that correlate microscale features to macroscale mechanical behaviors. An image of the setup under a stereomicroscope is presented in Fig. 1A. The main components of the setup are labeled in the simplified schematic (Fig. 1B). The gripping assembly consists of two blocks, a moving end and a fixed end. These form two grips that hold onto the two ends of the specimen using a gluing or clamping method. Sample deformation is produced by the displacement of the moving end holding one of the grips. This is powered by a motorized stage. The moving grip includes a load cell (Fig. 1B) that bends depending on the resistance of the sample to deformation. The load cell could be mounted on either gripping end. The fixed gripping end consists of three manual translation stages that are assembled into a three-axis stage to allow fine alignment of the sample along x, y, and z directions. The three-axis assembly is mounted on a rail mechanism that allows further adjustment of the gap between fixed and moving ends to accommodate a wide range of sample lengths. Various attachments can be mounted on the gripping ends to accommodate samples with diverse geometries and sizes. In our case, the main attachments

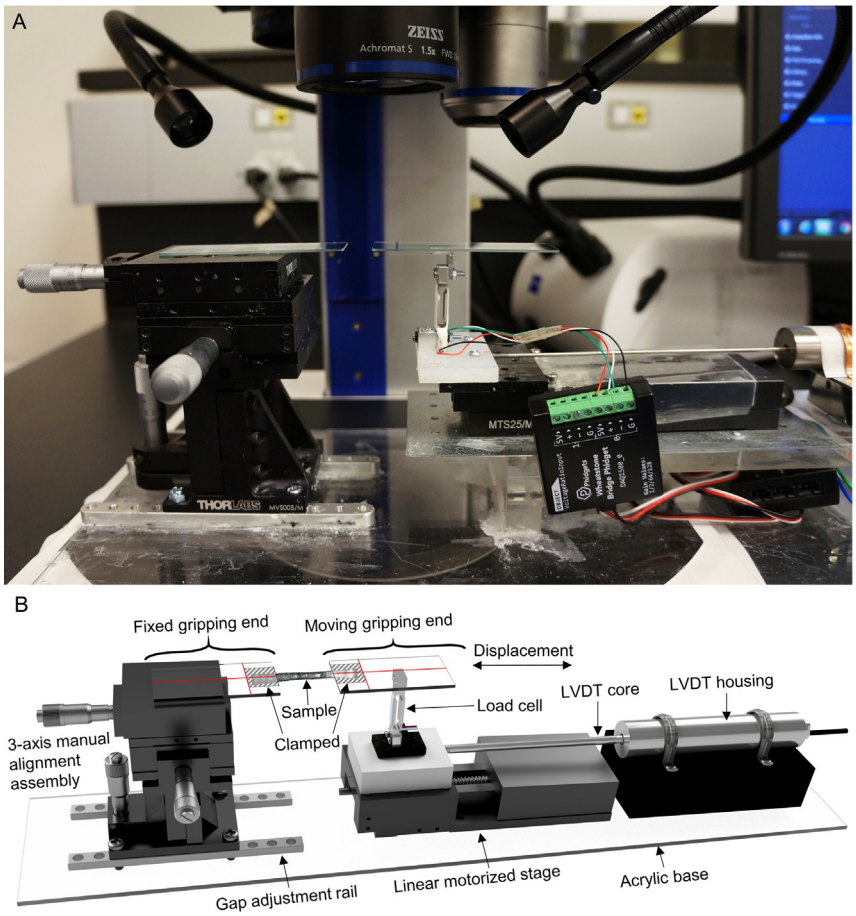

FIG. 1

Tensile testing device. (A) Tensile testing device placed under a stereomicroscope allowing real-time observation of tissue deformation at cell and tissue levels. (B) Schematic of the tensile testing device with the components labeled.

are microscope glass slides cut to a suitable size. A linear variable differential transformer (LVDT) serves as a position sensor to measure the displacement of the moving end. In the next section, details for each component of the device are provided.

4 Requirements

The setup relies on three main modules: a device to perform the mechanical test, a microscope to monitor the testing procedures, and a computer to run programs for the microscope and the tensile device. In this section, the hardware and software components of all three modules are specified.

4.1 Hardware requirements

4.1.1 Microscopy

The testing device presented in this chapter is designed with dimensions suitable for use with a Zeiss SteREO Discovery.V8 (Carl Zeiss) microscope (Fig. 2A). This microscope offers a long working distance which provides substantial flexibility for sample manipulation and test conditions. The microscope is equipped with three objectives (0.63×, 1.5×, 3.5×) and a manual 8× zoom. Images are captured by an attached digital color camera, AxioCam MRc R3 (Carl Zeiss), which is interfaced with the computer through an IEEE 1394a FireWire connection. The present setup can be scaled depending on the experimental needs and available resources to fit various types of microscopes. For microscopes with shorter working distances, smaller components may be necessary to build the device. This generally translates to an increased price and requires more sophisticated handling.

4.1.2 Computer

A desktop computer is used to run the software for microscopy, controlling the motorized stage and sensor data acquisition. The computer specifications used here were Windows 7 Professional 64-bit operating system with 24 GB of RAM, Intel Core i5-4670 CPU, 3.4 GHz, and AMD FirePro V4900 graphics card.

4.1.3 Tensile device

4.1.3.1 Linear motion stage

Controlled linear motion is a critical element of the tensile device. Linear motion can be generated through mechanisms including, but not limited to, (1) Linear motors which, instead of torque, provide direct linear force along the direction of displacement, (2) Servo (DC motor)/stepper motor-assisted rotational to linear motion, which can be achieved using rack and pinion or lead screw mechanisms, (3) Pneumatic or hydraulic linear actuators, and (4) Piezoelectric actuators. Each mechanism has advantages and drawbacks and several criteria must be considered when choosing the most suitable mechanism to generate linear motion for a particular application. These include the required load capacity, range of motion, precision (the minimum repeatable displacement), and environmental compatibility.

Actuator specifications typically involve a trade-off between travel range and precision. For example, piezoelectric actuators can provide a very high-precision linear displacement at the nanometer scale. However, this precision comes at the price of a low travel range. To satisfy the displacement requirements pertinent to tests at plant tissue scale, we used a commercially available DC servo-assisted motorized stage MTS25/M-Z8 (Thorlabs) (Fig. 2B). The stage has a working range of 25 mm, a maximum velocity of 2.4 mm/s, a maximum acceleration of 4.5 mm/s^2, a minimum repeatable incremental movement of 0.8 μm, a backlash of <6 μm, and maximum load capacities of 4.5 and 12 kg along vertical and horizontal directions, respectively. For control of the stage, we used a Brushed DC Motor Controller, KDC101 K-Cube (Thorlabs), which provides the option for both manual and computerized control (Fig. 2C).

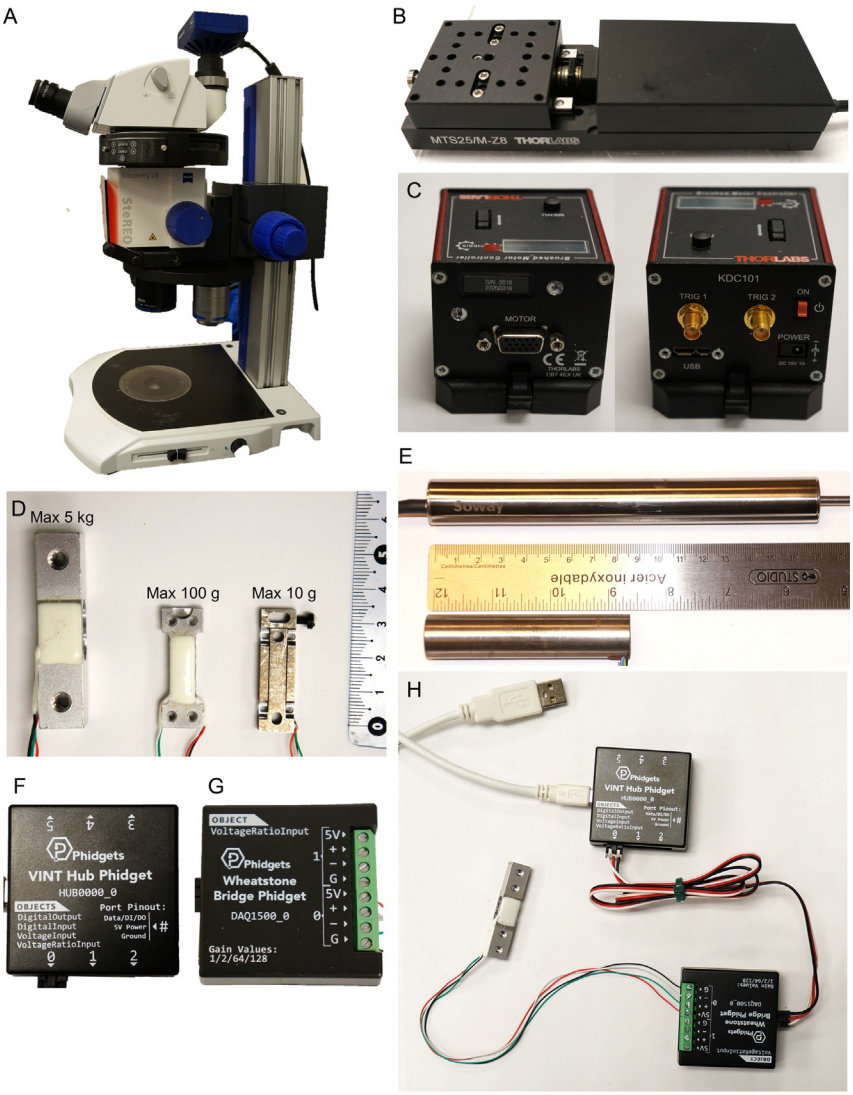

FIG. 2

Principal components of the tensile testing setup. (A) Stereomicroscope with large working distance accommodating the tensile testing device for real-time video-microscopy of the test procedures. (B) Commercially available linear motorized stage used to generate displacement of the moving gripping end of the tensile device. (C) Controller allowing both manual and computerized control of the motorized stage. (D) Three strain gauge-based load cells with different dimensions, load sensitivities and load capacities varying between 10 and 5000 g, all of which can be installed on the presented setup. (E) Two alternative LVDTs other than the one used on example setup (Fig. 1A). LVDTs can vary greatly in size and working range. (F) VINT Hub used for interfacing of computer and sensors to read data. (G) Wheatstone bridge circuit module used to amplify the signal from the load cell. (H) Load cell attached to the Wheatstone bridge and subsequently to the VINT Hub.

4.1.3.2 Force measurement

Force measurement is an integral part of quantitative mechanical characterization tests. Force sensors work by a wide range of mechanisms. Common force sensors include strain gauge-based, piezoresistive, pneumatic, hydraulic, inductive and reluctance types. The strain gauge-based load cells are a popular choice in many commercially available mechanical testing setups, including weighing systems. These load cells consist of a linearly elastic structure termed the spring element, such as a cantilever beam, onto which strain gauges are bonded. The deformation of the structure under external force produces a proportional change in the resistance of the circuits in the attached strain gauge. This small change in resistance can be accurately measured using a Wheatstone bridge circuit, where a given differential resistance produces an equivalent differential voltage. Strain gauge-based load cells can vary greatly in the shape of their deforming element, the type of measurement (e.g., compressive, tensile) they are capable of, and the magnitude of forces they can sense. Different shapes and deformation modes of the deforming elements in load cells include button, S-shaped, shear, and bending beam mechanisms. The present setup uses a single point shear beam load cell. Examples of three load cells of this type that can be used interchangeably on the present setup are shown in Fig. 2D, ranging from 10 g to 5 kg in their maximum load capacity. Similar to the actuators, there is generally a trade-off between the measurement range and the sensitivity of force sensors. Calibration is required to establish the correlation between the deformation of the spring element under a load/force and the output differential voltage data. In the example build, the shear beam commercial force sensor is Phidgets CZL639HD (Fig. 1A). This low-cost load cell has a maximum load capacity of 100 g (~1 N) and can operate within 3–10 V DC (VDC). The sensor has a rated output of 600 μV/V. This means that, at full load (100 g), the load cell generates 600 μV per each Volt of excitation. We operated the sensor at 5 VDC, which would produce 3000 μV signal data at full (100 g) load. Therefore, to achieve 1 g resolution, we required <30 μV data reading sensitivity. The Phidgets Wheatstone bridge board we used for force sensor data acquisition is reasonably sensitive (0.119 μV/V bridge voltage resolution, without gain). However, considering that the force sensor itself also has a relatively large rated output error of 150 μV/V, we could register weights/loads close to 0.5 g with good confidence. We found this load cell to be suitable for forces arising during tensile testing of onion epidermis. However, depending on the experimental needs, the use of load cells with considerably different load capacity and sensitivity might be necessary, which is possible due to the simple and flexible design of the apparatus.

4.1.3.3 Displacement measurement

Displacement measurement is indispensable in most mechanical tests, because it allows quantification of the strain that the specimen experiences under load. As with force measurement, various methods are available including strain gauges, potentiometers, capacitive sensors, and LVDTs. The linear motorized stage that we used to

generate linear motion is very precise (minimum achievable displacement increment of 0.05 μm and bidirectional repeatability of ~1.5 μm), but certain conditions can cause a significant input-output mismatch. For instance, overloading may cause the motor to miss steps, resulting in a difference between the prescribed (input) and the actual displacements. Further, in cyclic loading, the time required for the stage to reverse the direction of its movement at the end of the cycle results in a delay and a mismatch between actual and prescribed positions at each time point. Such delays accumulate over cycles, progressively worsening the temporal mismatch. Therefore, it is desirable to measure the displacement of the moving gripping end independently of the programmed displacement fed to the stage. For this purpose, this build uses a DC LVDT. LVDTs can operate on AC or DC power. While the AC and DC LVDTs have differences in their internal compartments, in both the displacement of a ferromagnetic core in or out of the cylindrical enclosure of the LVDT results in a detectable and proportional voltage differential at the output (Fig. 1B). In the apparatus used here, the moving core is attached to and moves with the linear motorized stage that accommodates the load cell and the moving gripping end assembly. LVDTs are mechanically resilient, have a theoretically infinite displacement resolution and a low hysteresis. LVDTs come in various sizes. In addition to the one used (Fig. 1A), two other LVDTs with different size and operation range are presented in Fig. 2E. Using a smaller LVDT allows more compact builds suitable to operate on a confocal microscope. Larger LVDTs, on the other hand, provide a larger working range, making them suitable to use with samples of different sizes, and eliminating the need to change parts between experiments. The working range-resolution trade-off generally does not apply to LVDTs as they have a theoretically infinite resolution, bound in practice by the resolution of the mechanical displacement mechanism and the data acquisition blocks. The LVDT model used in the example setup here, TRANS-TEK 0246-0000 J-02, has a ±76.2 mm working range, 6 (min)–30 (max) VDC excitation voltage. For proper operation, a minimum impedance of 50 kΩ is required. We used a controlled 15 VDC to excite the LVDT.

4.1.3.4 Computer interfacing of force and position sensors

Computer interfacing of the sensors is achieved using a VINT (Versatile Interface) HUB (ID: HUB000_0, Phidgets), which allows interfacing of 6 input/output devices through a single USB port (Fig. 2F). In our tensile device, we only require force and displacement sensors to be interfaced with the computer; therefore, two I/O ports are used. Each port on the VINT Hub can perform four functions: communicating with an intelligent VINT device, reading ratiometric sensor or voltage (0–5 VDC) data, reading switches and acting as a digital output. The displacement data from LVDT are read as voltage (0–5 VDC) whereas the force sensor data are read through a Phidgets DAQ-1500 Wheatstone bridge board (Fig. 2G and H). The Phidgets

Wheatstone bridge board used here has a 24-bit ADC (analog to digital converter), which is suitable to amplify and accurately measure the sensor output voltage at a resolution of 59.6 nV/V.

4.1.3.5 Power source

The LVDT is excited at a constant voltage of 15 VDC using a DC power supply (KD3005D digital-control, Korad) (Fig. 3A). For the present study, the VINT Hub was powered by a 5 V supply through the USB connection cable to the computer. The Phidgets Wheatstone bridge board was powered by the 5 VDC from the output of VINT Hub, and the load cell by the Wheatstone bridge board.

4.1.3.6 Three-axis manual alignment stage

For maximum control of sample alignment between the two grips, a manual three-axis stage is used at the fixed gripping end. Two horizontal stages (Fig. 3B) that allow displacement in x and y directions (MT1/M, Thorlabs) and a third stage enabling z displacement (Thorlabs, MVS005/M) are used for manual alignment. The horizontal and vertical stages have travel ranges of 12.7 and 13 mm, respectively. In both stages, the displacement adjustment is performed through rotation of a micrometer that delivers a 500 µm translation per revolution with a resolution of 10 µm allowing both coarse and fine sample alignment corrections in x, y, and z.

4.2 Software

4.2.1 Microscopy software

The live mode of Zen 2.3 (blue edition) software (Carl Zeiss Microscopy GmbH) is used for real-time monitoring of sample mounting and tensile testing procedures under the stereomicroscope. Real-time monitoring can provide valuable information including the detection of preexisting defects in the sample, sample misalignment, and occurrence of sample slippage during the tension test. The freely available open-source software µManager can be used for this purpose as well. To capture videos, we found it efficient to record the screen using the screen capture software SnagIt (TechSmith) while running the Zen software on Live mode.

4.2.2 Tensile device software

4.2.2.1 Control of motorized stage

Thorlabs APT user 3.3.6379.18353 application is used to communicate with the hardware controller to control the displacement of the MTS25/M-Z8 Thorlabs linear motorized stage. The APT user interface allows specifying detailed movement for the motorized stage, such as speed, acceleration and dwell time, creating different types of loading and unloading scenarios (Fig. S1 in the online version at https://doi.org/10.1016/bs.mcb.2020.04.003).

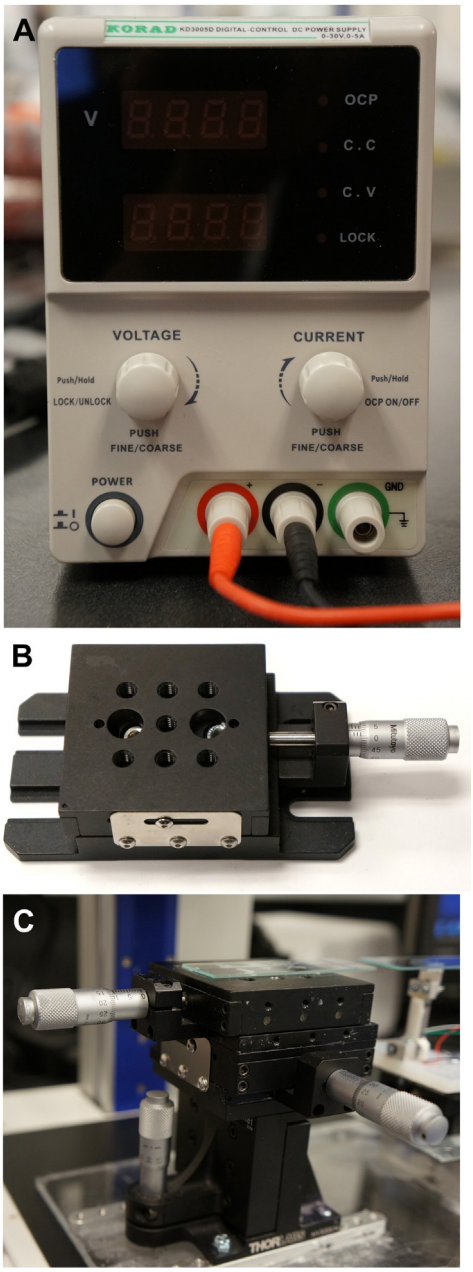

FIG. 3

Secondary components of the tensile testing setup. (A) Laboratory AC to DC power supply used to power the LVDT position sensor. (B) Manual linear stage allowing fine horizontal positioning. (C) Assembly of two horizontal and a vertical manual translation stages into a three-axis stage on which the fixed sample gripping end is mounted.

4.2.2.2 Acquisition and registration of sensor data

A custom Python script is used to read the signal acquired at the computer from the VINT Hub, and to convert it to displacement and force data (see the.py file in the Supplementary data 1 in the online version at https://doi.org/10.1016/bs.mcb.2020.04.003 or on github at https://github.com/Bidhendi/MTP). The code plots force-displacement data on the screen in real time, and saves data in a .csv file as well. The script is compatible with Python 2.7.1 and is developed using Python (x,y) software (https://python-xy.github.io) with the Spyder (2.3.5.2) interactive scientific development environment for editing and debugging. There are several other Python distributions and editors that can be used to modify and run the script.

5 Device assembly

Besides the electrical wiring and the computer interfacing, the tensile testing device assembly is composed of five blocks (Fig. 1A and B): (1) Base block, (2) Motorized stage, (3) Force sensing block, (4) Displacement sensing block, and the (5) Sample mounting three-axis static block. A rectangular piece of an acrylic sheet is used as a portable substrate onto which other components are mounted. The thickness needs to be sufficient to allow inserting screws for proper attachment of parts and to withstand the weight of the components for portability. A 0.5 cm thick acrylic sheet is used here. The motorized stage is fixed on the acrylic base, and the force-sensing block is attached to it. The force sensing block consists of a force sensor with an extension used to facilitate sample gripping. For displacement sensing, the movable ferromagnetic core of the LVDT is attached to the moving gripping end assembly mounted on the motorized stage. Through precise horizontal positioning, the core "floats" freely and moves without contact with the inside of the cylindrical enclosure. The enclosure is fastened, through an intermediate block, to the base using strap clamps. The fixed gripping end, as mentioned before, consists of a three-axis manipulation system and a hard and flat surface (in our case, we used standard microscope slides). The manual translation stages are screwed together and the whole assembly is screwed to a rail mechanism glued to the acrylic base (Fig. 3C).

For control of the motorized stage and for sensor data acquisition, the whole assembly is interfaced with a computer. The motorized stage is controlled by the Thorlabs controller using a USB cable. Similarly, a USB interface is used for the data acquisition through the VINT Hub, which acts as the centerpiece connecting both the force and displacement sensors to the computer. For details on part connections and wiring, with the example modules mentioned in this chapter, see Fig. 4.

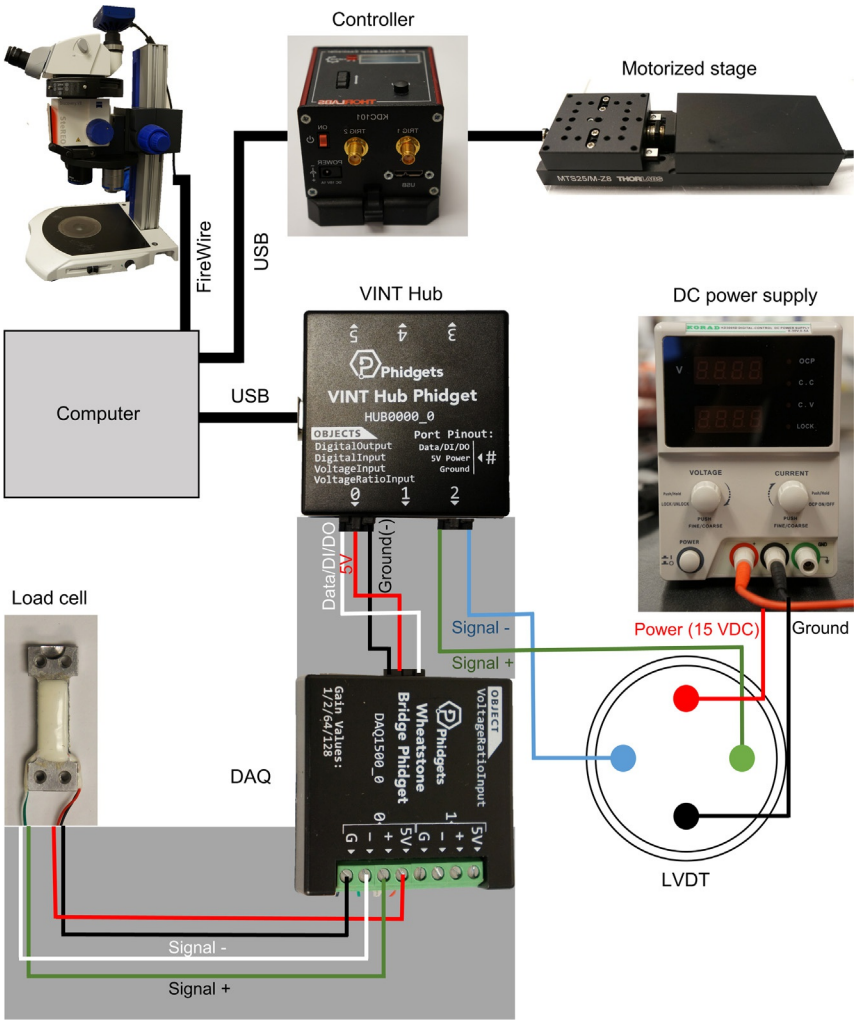

FIG. 4

Illustration of the connections between the components used in the example device setup. The components can be changed, and different actuation and sensing mechanisms can be used depending on the force, displacement, sensitivity and size requirements. The present connections are for the parts used in this example. Other modules may have different requirements and the manufacturer data sheets must be consulted before assembly.

6 Device calibration

Sensors need to be calibrated prior to use. The calibration procedure aims at establishing a precise relationship between the sensor input (such as the force applied on a load cell or the displacement imposed on the LVDT core) and the output signal.

Here, strain gauge-based load cells are used which transduce mechanical strain resulting from the application of an external force to a change in their output voltage. Different methods are available for calibration of load cells. Here, known weights are affixed to the load cell with the sample-mounting extensions attached as in the actual experiments. A precision laboratory scale (here A&D, ER-180A) is used to determine the weights of calibration objects. Since some load cells are sensitive to the direction of load application (e.g., tension or compression), the direction of affixing the calibration mass should be the same as the direction of the loads exerted in the actual experiments. The values for output voltage are plotted against the applied weights (force) and a linear regression is performed. A linear function is used to correlate the applied load and the output signal:

$$W(S) = aS + b \tag{1}$$

A line in 2-dimensional space can be characterized by a slope, a, and a y-intercept, b, as in Eq. (1). Here, S is the sensor output signal and $W(S)$ is the force equivalent of that signal. In the example provided here (Fig. S2 in the online version at https://doi.org/10.1016/bs.mcb.2020.04.003), we use directly the value of calibration weights in gram-force. Conversion to other force units (e.g., Newton) can be performed any time prior to calibration or after that during the analysis of experimental results if needed. Using a line function for correlating the force and signal assumes that the load cell deforms linearly with the applied weight and that the signal changes linearly with deformation. We observed the load cells used here to behave linearly over their load capacity range (Fig. S2 in the online version at https://doi.org/10.1016/bs.mcb.2020.04.003). In the case of non-linear behavior, calibration is still possible but requires using a nonlinear function to describe the load cell behavior (instead of the linear function in Eq. (1)). Detailed steps for calibration are as follows and calculations are presented in Fig. S2 in the online version at https://doi.org/10.1016/bs.mcb.2020.04.003:

1. For consistent calibration and mounting of the samples during actual experiments, a longitudinal centerline is marked on both moving and non-moving gripping ends. The thread used to affix calibration masses is aligned with this line (Fig. 5A). Fig. 5 shows only the moving gripping end of the tensile device which includes the load cell. A horizontal line is also marked on the glass slides, demarcating the location of the end of the sample, and that of the hanging thread during calibration.
2. A Python script (.py file provided as Supplementary data 1 in the online version at https://doi.org/10.1016/bs.mcb.2020.04.003) is used to record and to visualize in real-time on the screen the signal values from the sensors.
3. We found that attaching masses to the load cell extension in the horizontal position using a thread can be problematic, as the friction between the thread and the assembly can affect the load transmitted to the sensor. Therefore, calibration is performed vertically with the device held in upright position (Fig. 4B). A spirit level can be used to ensure the device is leveled.

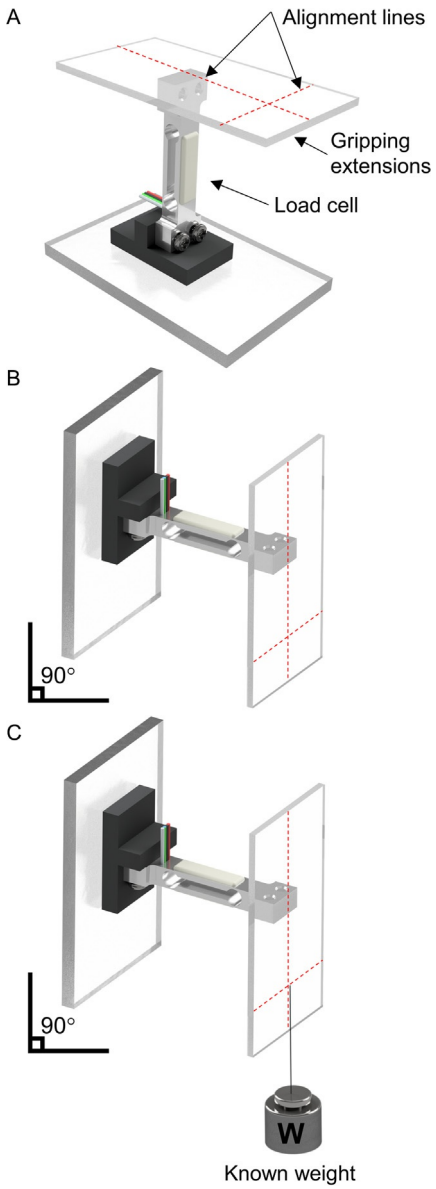

FIG. 5

Steps in the calibration of the force sensor of the tensile device. (A) Load cell signal recorded with the device in horizontal (working) position. (B) Load cell with the device in the vertical configuration. The signal is the sum of the zero-balance and dead load (of gripping extension) signals. (C) Affixing known weights to the load cell extension produces data points for the calibration of the load cell.

For calibration for a tensile test, the load cell must be loaded downward in this position towards the to-be-attached sample. To use the device for a compression test, the loading direction (and generally that of the load cell) must be reversed.

4 First, the output of the load cell is noted in the horizontal position, S_0, and entered in an Excel file (Figs. 4A and S2 in the online version at https://doi.org/10.1016/bs.mcb.2020.04.003). The weight corresponding to this configuration is noted as zero.

5 The device is then put in vertical position as explained in step 3 (Fig. 5B) and the signal value in this position (S_d) is recorded and entered in the calibration Excel file (Fig. S2 in the online version at https://doi.org/10.1016/bs.mcb.2020.04.003). This signal entails the effect of the dead weight of the load cell and the extension assembly (W_d, the index d refers to dead weight).

6 A known weight (W_1) is affixed to the load cell assembly (Fig. 5C). A thread with a negligible weight is used for suspending the mass (0.1 g or less for a piece of wire that is used as suspension thread). The weight of the thread can also be measured and counted towards the calibration weight. The signal (S_1) is due to both the suspended weight (W_1) and the dead weight (W_d). This signal is noted and entered in the calibration Excel file (Fig. S2 in the online version at https://doi.org/10.1016/bs.mcb.2020.04.003).

7 A second known weight (W_2) is suspended from the load cell, as in the previous step, and the signal S_2 is recorded. This step can be repeated to produce the desired number of data points for calibration (in Fig. S2 in the online version at https://doi.org/10.1016/bs.mcb.2020.04.003 we used four weights).

8 The ratio C correlating changes in the output signal with changes in applied weight is calculated (see Fig. S2 in the online version at https://doi.org/10.1016/bs.mcb.2020.04.003). For two known weights this is done by calculating:

$$C = (S_2 - S_1)/(W_2 - W_1) \tag{2}$$

In case that multiple weights are used for calibration, C can also be calculated by finding the inverse of the slope of the regression line passing through those data points.

9 With C from Eq. (2), the dead weight, W_d, can be calculated:

$$W_d = (S_d - S_0)/C \tag{3}$$

10 The dead weight calculated from (3) is used to update the actual weight values affixed to the load cell in the vertical position. Actual weights are the sum of the weight of the suspended mass plus the dead weight, see Fig. S2 in the online version at https://doi.org/10.1016/bs.mcb.2020.04.003.

11 Signal values are plotted against calibration weight (weight for the horizontal position is assumed as zero), and the slope and the y-intercept of the regression line fitting the data are determined (a and b of Eq. (1)). The goodness of the fit and the assumption of linearity can be observed in the result (Fig. S2 in the online version at https://doi.org/10.1016/bs.mcb.2020.04.003).
12 Upon completing the calibration, the identified values from step 11 are entered in the Python script.
13 To test the calibration, the force output in the horizontal position must read a value close to zero (allowing minor deviations due to factors such as noise). In the vertical position, when unloaded, the force should show a value close to the dead weight calculated in step 9. Further checks can be performed by affixing known weights within the load capacity of the load cell. If the readings are not reasonably consistent with the calibration curve, the calibration procedure needs to be reexamined.

If the fixtures or the type of experiment (compression, three-point bending, tensile test, etc.) are changed, the calibration procedure must be repeated. Further, a force sensor is subject to performance alterations due to wear and tear, aging or exposure to excessive loads. Some types of load cells are also susceptible to environmental changes such as temperature. Therefore, routine calibration of force sensors is recommended prior to each set of experiments, even if the fixtures have remained unchanged from prior experiments.

The position sensor, the LVDT, also needs to be calibrated. As mentioned previously, the displacement of the magnetic core within the cylindrical enclosure of the LVDT produces a voltage differential proportional to the displacement. However, the output signal from the LVDT depends on several parameters, including its build and the excitation voltage. Therefore, before experimentation, one must calibrate the LVDT at the excitation voltage that will be used during the actual experiments. Various methods can be used for calibration, such as affixing a micrometer device to the LVDT. Here, we performed the calibration by comparing the LVDT output signal with the displacement fed to the motorized stage to which the moving core is attached. The displacements are fed to the motorized stage through the APT user interface. The accuracy of the displacement of the motorized stage itself is assessed by measuring the displacement of a fiducial marker on the stage under the stereomicroscope. A linear function such as the one in the Eq. (1) is used for calibration. The Python script can be used to display the output signal of the LVDT on screen. The output signals and the core position are read for a number of successive displacement increments of the motorized stage and are entered in an Excel file. The equation of the line passing through the data pairs provides the slope and the y-intercept of the line (see Fig. S3 in the online version at https://doi.org/10.1016/bs.mcb.2020.04.003). These values are then entered in the corresponding line of the Python script.

7 Example of tensile tests on plant tissue using onion epidermis

To illustrate the use of this mechanical testing apparatus, we present an example tensile test on a segment of onion epidermis. Sample preparation and testing were performed according to descriptions provided by Bidhendi, Li, and Geitmann (2019).

1. The tensile device was calibrated, as explained in the previous section, with the affixed extensions to ensure accurate force reading. Therefore, when in the horizontal position and prior to the test, a force value close to zero was expected.
2. The desired pattern and amplitude of the displacement of the motorized stage were input in the APT user interface. In this example, a two-cycle loading-unloading protocol was programmed. The free length of the clamped sample was 12 mm. The first cycle was set to apply a stretch of 2.5 mm, corresponding to a strain of approximately 20% of the original length of the sample). Upon returning to mechanical zero, the program was set to start a second cycle by applying a stretch of 9 mm (i.e., 75% strain). From experience, we knew that this value is above the strain at which most onion strips fail (typically 50%) (Bidhendi, Li, & Geitmann, 2019). The speed of grip displacement was set to 20 μm/s.
3. The tensile testing samples were epidermal peels from fresh onion (*Allium cepa* L.) scales. The peels were taken from the adaxial epidermis, the readily detachable epidermis located on the inner side of an onion scale. The elongated segments used here were excised from the region between the equator and pole of an onion scale (oriented parallel to the equator).
4. Cutting of samples has to be performed in a consistent manner. Here, we used a custom cutter that allows cutting elongated tissue segments with tapered ends. The tapered ends help with gripping of the sample reducing slippage (Bidhendi, Li, & Geitmann, 2019). The cutter was pressed onto a piece of the onion scale positioned on polystyrene foam. The soft polystyrene substrate allows the blade to pass through the entire scale cookie-cutter style, ensuring a perfectly shaped cut and easy removal of the epidermis segment from the scale eliminating uncontrolled tearing of the sample during detachment (Fig. 6A). The epidermal strip was then detached off the surface of the scale segment with a gentle pulling movement using a tweezer.
5. The epidermal strip was submerged in a 0.8 mol/L mannitol solution for 15 min to remove turgor, and its ends were subsequently mounted on the glass slides serving as the bed for gripping ends of the tensile device (Fig. 6B).
6. The sample was clamped using spring clamps. The sample should be mounted stress-free. This means that mounting and clamping should not cause a stretch in the sample prior to the beginning of the test.
7. A few drops of the proper solution, in this case, mannitol, was spread over the sample to keep it hydrated, using a disposable pipette.

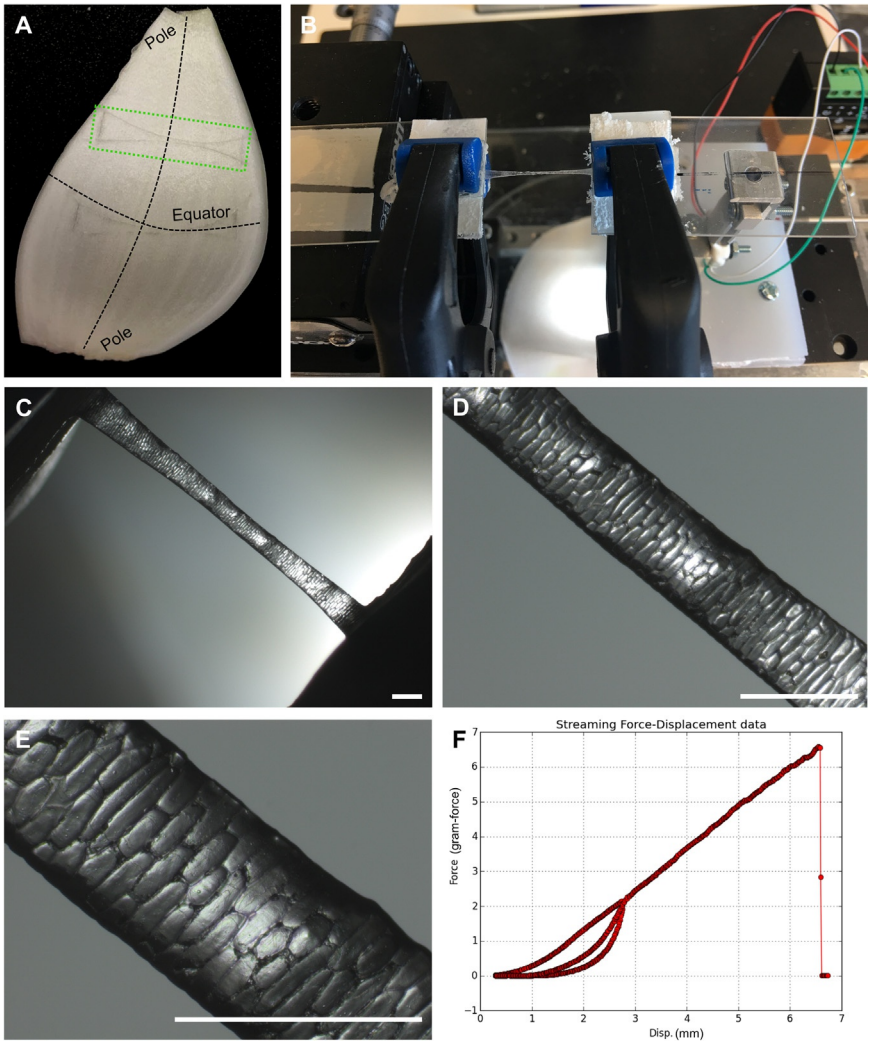

FIG. 6

Example tensile test performed on the adaxial epidermis of onion. (A) Tapered segment of adaxial onion epidermis excised parallel to the onion equator. (B) Sample mounted on gripping jaws, using spring clamps. (C, D, E) Sample can be observed at different magnifications during the tensile test. (F) The force-displacement graph of the tensile test performed for two cycles with a first cycle up to 20% strain followed by a larger strain cycle leading to sample failure. Permanent deformation upon unloading at the end of the first cycle and hysteresis (loading and unloading following different paths) can be observed. Scale bars = 1 mm.

8. Upon start of live mode microscopy and capturing the on-screen events, the tensile test was initiated by first running the Python script to register the signals, and then the motorized stage to perform cyclic loading based on the above-mentioned input cycles through the APT user interface.
9. During the test, a few more drops of the solution were gently dispersed over the sample without disturbing the test or causing noticeable noise in the visualized force data output. A good occasion to do this can be at the end of the first cycle when the moving grip has returned to mechanical zero and the force is nearly zero. The sample was monitored microscopically at various magnifications during the test (Fig. 6C–E). An example of the force-displacement data for the sample depicted in Fig. 6C–E is shown in Fig. 6F. We implemented measures to eliminate or minimize slippage including the use of sandpaper between the clamp and the sample. Sample slippage can lead to local oscillations in force. When sample slippage is detected, either during or after the experiment and during the analysis of data, the experimental data beyond the onset of noticeable slippage is not useful and should be discarded. Oscillations can also be caused by micro-damages (e.g., rupture of a cell wall segment) in the sample, resulting in repeated small reduction in the amount of load-bearing material leading to force oscillation. In this latter case, the phenomenon is indicative of irreversible damage in the specimen, which is to be expected in specimens strained to rupture. If oscillations occur due to this phenomenon, the experimental data can still be used for interpretation of the mechanical parameters. In the case of a plant tissue, cell wall segments do not all fail at the same time and local damage in the specimen can begin well before complete rupture occurs. When rupture is not intended, strain magnitudes must therefore be chosen carefully and the appropriate elastoplastic model for interpreting the tensile test data must be used.
10. Upon termination of the experiment, the data files were moved to a separate folder and saved for future analysis, for instance for calculation of the elastic modulus. Supplementary Movie 1 in the online version at https://doi.org/10.1016/bs.mcb.2020.04.003 provides a screen capture of a tensile test on an adaxial onion epidermal strip.

8 Considerations and possible improvements

The costliest elements in the presented design are the linear motion stages, especially the motorized one. An in-house linear motion stage built, for instance, by combining a stepper motor with a fine ball screw, can be used as an alternative to commercial translation stages allowing further customization and reduction of the expenses. Regardless of this, the total cost of the apparatus constitutes a fraction of the comparable commercially available systems. The present setup is versatile and scalable. While introduced as a tensile tester, the gripping attachments and loading direction

can be modified to perform other types of mechanical tests, such as three or four-point bending protocols. The fixtures forming the grips can be 3D printed. Considerably more compact builds are possible by choosing smaller parts, allowing device dimensions suitable for cell developmental studies requiring higher magnification and microscopy techniques that permit only small working ranges. Lower forces are measurable using more sensitive load cells than the 100 g load cell used in this example, but at exponentially increasing part and design expenses.

Adopting proper statistical measures and ensuring data reproducibility (Nelson, Stubbs, Larson, & Cook, 2019) are essential for meaningful mechanical characterization of plant samples. Experimental design considerations also comprise component specifications that are provided by the manufacturer or need to be calculated by the user. Some of the terms that users need to familiarize themselves with include accuracy, precision, resolution, sensitivity, repeatability, reproducibility, various errors, linearity, hysteresis, creep, and maximum range/load and maximum overload (Norden, 1998). For safe and reliable usage and measurement, these parameters should be respected. For instance, loading the force sensors beyond their maximum capacity can result in nonlinear behavior, damage and eventually mechanical failure. Different sources may use some of these terms interchangeably or attribute slightly different meanings.

In the present setup, sample strain is calculated based on the displacement of the moving grip measured by the LVDT. However, sample elongation is not necessarily always equal to grip displacement. This differential can result from sample slippage at the grip, a commonly encountered challenge in tensile testing. Slippage leads to a smaller degree of sample elongation than the displacement of the grip would indicate, leading to the calculation of erroneous strain values. Various methods are devised for more accurate and informative strain measurements, such as the use of non-contact strain measurement methods, e.g., optical extensiometry. The structural compliance of the tensile device proper can also contribute to error in measured strain, as the machine parts can move, bend and deform along with the sample, an effect that must be corrected for (e.g., Kalidindi, Abusafieh, & El-Danaf, 1997). Lastly, the Python script provided along with this chapter can be developed further, enabling more sophisticated loading protocols that, for example, require force-displacement feedback, as in constant load or constant elongation tests.

Acknowledgments

This study was supported by a Discovery grant from the Natural Sciences and Engineering Research Council of Canada (NSERC) and by the Canada Research Chairs Program. We would like to also acknowledge Dr. Hongbo Li (College of Engineering, Shanxi Agricultural University) who performed the example test presented in this chapter during his visit to McGill. We apologize to colleagues whose relevant works are not cited due to space constraints.

References

Berthaume, M. A. (2016). Food mechanical properties and dietary ecology. *American Journal of Physical Anthropology*, *159*, 79–104.

Bidhendi, A. J., Altartouri, B., Gosselin, F. P., & Geitmann, A. (2019). Mechanical stress initiates and sustains the morphogenesis of wavy leaf epidermal cells. *Cell Reports*, *28*, 1237–1250.

Bidhendi, A. J., & Geitmann, A. (2016). Relating the mechanics of the primary plant cell wall to morphogenesis. *Journal of Experimental Botany*, *67*, 449–461.

Bidhendi, A. J., & Geitmann, A. (2018a). Finite element modeling of shape changes in plant cells. *Plant Physiology*, *176*, 41–56.

Bidhendi, A. J., & Geitmann, A. (2018b). Tensile testing of primary plant cells and tissues. In A. Geitmann & J. Gril (Eds.), *Plant biomechanics* (pp. 321–347). Springer Verlag: Cham.

Bidhendi, A. J., & Geitmann, A. (2019). Methods to quantify primary plant cell wall mechanics. *Journal of Experimental Botany*, *70*, 3615–3648.

Bidhendi, A. J., Li, H., & Geitmann, A. (2019). Modeling the nonlinear elastic behavior of plant epidermis. *Botany*, *98*, 49–64.

Chanliaud, E., Burrows, K. M., Jeronimidis, G., & Gidley, M. J. (2002). Mechanical properties of primary plant cell wall analogues. *Planta*, *215*, 989–996.

Cosgrove, D. J. (1993). Wall extensibility: Its nature, measurement and relationship to plant cell growth. *New Phytologist*, *124*, 1–23.

Cosgrove, D. J. (2014). Re-constructing our models of cellulose and primary cell wall assembly. *Current Opinion in Plant Biology*, *22*, 122–131.

Cosgrove, D. J. (2016). Plant cell wall extensibility: Connecting plant cell growth with cell wall structure, mechanics, and the action of wall-modifying enzymes. *Journal of Experimental Botany*, *67*, 463–476.

Davis, J. R. (Ed.), (2004). *Tensile Testing*. (2nd ed.). Materials Park, Ohio: ASM international.

Forell, G. V., Robertson, D., Lee, S. Y., & Cook, D. D. (2015). Preventing lodging in bioenergy crops: A biomechanical analysis of maize stalks suggests a new approach. *Journal of Experimental Botany*, *66*, 4367–4371.

Kalidindi, S., Abusafieh, A., & El-Danaf, E. (1997). Accurate characterization of machine compliance for simple compression testing. *Experimental Mechanics*, *37*, 210–215.

Lynch, T. M., & Lintilhac, P. M. (1997). Mechanical signals in plant development: A new method for single cell studies. *Developmental Biology*, *181*, 246–256.

McQueen-Mason, S., Durachko, D. M., & Cosgrove, D. J. (1992). Two endogenous proteins that induce cell wall extension in plants. *The Plant Cell*, *4*, 1425–1433.

Milani, P., Braybrook, S. A., & Boudaoud, A. (2013). Shrinking the hammer: Micromechanical approaches to morphogenesis. *Journal of Experimental Botany*, *64*, 4651–4662.

Milani, P., Gholamirad, M., Traas, J., Arnéodo, A., Boudaoud, A., Argoul, F., et al. (2011). In vivo analysis of local wall stiffness at the shoot apical meristem in *Arabidopsis* using atomic force microscopy. *The Plant Journal*, *67*, 1116–1123.

Nelson, N., Stubbs, C. J., Larson, R., & Cook, D. D. (2019). Measurement accuracy and uncertainty in plant biomechanics. *Journal of Experimental Botany*, *70*, 3649–3658.

Norden, K. E. (1998). *Handbook of electronic weighing*. Weinheim: Wiley-VCH.

Pelling, A. E., & Hickey, R. J. (2019). Cellulose biomaterials for tissue engineering. *Frontiers in Bioengineering and Biotechnology*, *7*, 45.

Robinson, S., & Durand-Smet, P. (2020). Combining tensile testing and microscopy to address a diverse range of questions. *Journal of Microscopy*. https://doi.org/10.1111/jmi.12863.

Robinson, S., Huflejt, M., de Reuille, P. B., Braybrook, S. A., Schorderet, M., Reinhardt, D., et al. (2017). An automated confocal micro-extensometer enables in vivo quantification of mechanical properties with cellular resolution. *The Plant Cell*, *29*, 2959–2973.

Routier-Kierzkowska, A.-L., & Smith, R. S. (2013). Measuring the mechanics of morphogenesis. *Current Opinion in Plant Biology*, *16*, 25–32.

Sharpe, W. N. (Ed.), (2008). *Springer handbook of experimental solid mechanics*. New York: Springer.

Spatz, H., Kohler, L., & Niklas, K. (1999). Mechanical behaviour of plant tissues: Composite materials or structures? *Journal of Experimental Biology*, *202*, 3269–3272.

Suslov, D., & Verbelen, J. (2006). Cellulose orientation determines mechanical anisotropy in onion epidermis cell walls. *Journal of Experimental Botany*, *57*, 2183–2192.

Tagawa, T., & Bonner, J. (1957). Mechanical properties of the *Avena* coleoptile as related to auxin and to ionic interactions. *Plant Physiology*, *32*, 207.

Vanstreels, E., Alamar, M., Verlinden, B., Enninghorst, A., Loodts, J., Tijskens, E., et al. (2005). Micromechanical behaviour of onion epidermal tissue. *Postharvest Biology and Technology*, *37*, 163–173.

Vega-Sánchez, M. E., Verhertbruggen, Y., Christensen, U., Chen, X., Sharma, V., Varanasi, P., et al. (2012). Loss of *Cellulose synthase-like F6* function affects mixed-linkage glucan deposition, cell wall mechanical properties, and defense responses in vegetative tissues of rice. *Plant Physiology*, *159*, 56–69.

Wei, C., & Lintilhac, P. M. (2007). Loss of stability: A new look at the physics of cell wall behavior during plant cell growth. *Plant Physiology*, *145*, 763–772.

Wei, C., Lintilhac, P. M., & Tanguay, J. J. (2001). An insight into cell elasticity and load-bearing ability. Measurement and theory. *Plant Physiology*, *126*, 1129–1138.

Zamil, M. S., Yi, H., Haque, M., & Puri, V. M. (2013). Characterizing microscale biological samples under tensile loading: Stress–strain behavior of cell wall fragment of onion outer epidermis. *American Journal of Botany*, *100*, 1105–1115.

Zamil, M. S., Yi, H., & Puri, V. M. (2015). The mechanical properties of plant cell walls soft material at the subcellular scale: The implications of water and of the intercellular boundaries. *Journal of Materials Science*, *50*, 6608–6623.

Zhang, T., Tang, H., Vavylonis, D., & Cosgrove, D. J. (2019). Disentangling loosening from softening: Insights into primary cell wall structure. *The Plant Journal*, *100*, 1101–1117.

Zhang, T., Vavylonis, D., Durachko, D. M., & Cosgrove, D. J. (2017). Nanoscale movements of cellulose microfibrils in primary cell walls. *Nature Plants*, *3*, 1–6.